

Monolayer MoS₂ Nanoribbons as a Promising Material for Both *n*-type and *p*-type Legs in Thermoelectric Generators

A. ARAB,^{1,2,4} A.V. DAVYDOV,² D.A. PAPACONSTANTOPOULOS,³
and Q. LI¹

1.—Department of Electrical and Computer Engineering, George Mason University, Fairfax, VA, USA. 2.—Material Science and Engineering Laboratory, National Institute of Standard and Technology, Gaithersburg, MD, USA. 3.—School of Computational Sciences, George Mason University, Fairfax, VA, USA. 4.—e-mail: aarab@gmu.edu

First-principles calculations have been performed to study the thermoelectric properties of monolayer MoS₂ armchair nanoribbons (ACNRs). The electronic behavior of nanoribbons is dominated by the presence of edge states that are dependent on the number of zigzag chains across the nanoribbon. In addition, it is found that the phonon thermal conductance of monolayer MoS₂ ACNRs is smaller than monolayer films due to phonon edge scattering. This effect is more pronounced in narrower nanoribbons, which leads to a higher ZT value compared to a monolayer MoS₂ sheet. The effects of sulfur vacancy and edge roughness on the thermoelectric properties of MoS₂ ACNRs have also been studied. We found that edge roughness decreased ZT values compared to those of perfect nanoribbons, as its impact on electrical conductance is more severe than on phonon thermal conductance. Sulfur vacancy, however, improved ZT in some subbands. It is shown that ZT values as high as 4 for electron-doped and 3 for hole-doped nanoribbons can be achieved at $T = 500$ K. The ability to achieve high ZT values for both *p*-type and *n*-type nanoribbons makes monolayer MoS₂ ACNR a promising candidate for future solid-state thermoelectric generators.

Key words: Thermoelectric generation, MoS₂ Nanoribbon, seebeck coefficient, ZT

INTRODUCTION

Atomically thin two-dimensional (2D) materials have attracted a strong interest since the discovery of graphene.¹ Great strides have been made toward understanding graphene's interesting physical and electrical properties.^{2–4} However, the potential use of graphene in electronics applications has been hindered by the fact that it has zero band gap (E_g) in its pristine form. More recently, another family of 2D materials has emerged: transition metal dichalcogenides (TMDCs). Bulks of these materials are formed by layers vertically stacked and weakly bonded together via van der Waals forces. This weak interlayer interaction makes it possible to

obtain monolayers by using scotch tape exfoliation⁵ or lithium-ion intercalation⁶ techniques. In contrast to graphene with $E_g = 0$, some members of the TMDC family have an appropriate band gap for microelectronic applications. Molybdenum disulfide (MoS₂) is one of the most representative and intensively studied 2D TMDCs, in part due to its thermal stability and natural abundance.^{7–9} Bulk MoS₂ is an indirect gap semiconductor¹⁰ with $E_g = 1.2$ eV, while monolayer MoS₂ is a direct gap semiconductor¹¹ with $E_g = 1.8$ eV. The desirable band gap, good carrier mobility (which is close to those of silicon thin films and graphene nanoribbons),¹² excellent thermal stability, and a smooth surface free from dangling bonds,¹³ make MoS₂ a promising candidate for electronic and optoelectronic applications.¹⁴

(Received April 21, 2016; accepted June 2, 2016)

The thermoelectric properties of MoS₂ have not been as well studied as its electrical properties.^{15,16} The direct conversion of heat into electricity in thermoelectric materials is considered a solution for using wasted heat energy sources as renewable energy supplies, and hence, highly efficient thermoelectric materials and devices have attracted intensive interest. Performance of a thermoelectric material in converting heat into electricity can be evaluated by a figure of merit; $ZT = GS^2T/(\kappa_e + \kappa_{ph})$, in which G , S , T , κ_e and κ_{ph} are the electrical conductance, Seebeck coefficient, absolute temperature, electronic contribution to thermal conductance, and phonon contribution to thermal conductance, respectively. It is desirable to have a high electrical conductance and Seebeck coefficient and low thermal conductance to achieve a high ZT value. For conventional thermoelectric materials, e.g., PbTe¹⁷ and Bi₂Te₃-based alloys,¹⁸ ZT values of around 2.4 at $T = 900$ K were achieved. Further increase of ZT in these materials proved to be a challenge since the parameters that affect ZT are generally coupled with each other. Enhancement to one of them may degrade the other and the overall effect on ZT will neutralize. The situation did not change much until higher ZT values were shown in the low-dimensional^{19,20} and nanostructured thermoelectric materials,²¹ whereas their Seebeck coefficients were enhanced by quantum confinement and their thermal conductance were decreased by increasing phonon boundary scattering.²² Thermal conductivity can be further decreased by deliberately introducing surface roughness²³ and defects in materials.²⁴

The high Seebeck coefficient of 600 $\mu\text{V}/\text{K}$ at room temperature²⁵ reported for bulk MoS₂ is higher than that seen in most good thermoelectric materials. It was also reported that the Seebeck coefficient of MoS₂ can be tuned as high as 10⁵ $\mu\text{V}/\text{K}$ by imposing a gate electric field.²⁶ In addition, low thermal conductivity was also reported for MoS₂ thin films.^{27,28} Despite the reported high Seebeck coefficient and low thermal conductivity, bulk MoS₂ was predicted to have a low ZT value²⁹ of 0.1 at 700 K that could be attributed to its poor conductivity.^{25,30,31} High pressure was used in an attempt to tune interlayer interactions of bulk MoS₂, and its ZT increased to 0.65 over a wide range of temperature and pressure.³²

In addition, anisotropy in the thermal conductance³³ and ZT ³⁴ is reported in armchair and zigzag directions. In our previous study, we calculated ZT values of the 2D monolayer and few-layer MoS₂ sheets in both armchair and zigzag directions in a density functional theory (DFT) framework.³⁴ We showed that by increasing the number of layers, the ZT value decreased and also higher ZT values could be achieved in armchair as compared to zigzag MoS₂.³⁴ The highest ZT value was 1.2 for p -type armchair MoS₂ monolayers, which is in good

agreement with a previous report.³⁵ This represented a large ZT boost from bulk MoS₂.

By taking advantage of the higher boundary scattering, and hence lower thermal conductance, of one-dimensional (1D) nanoribbons in comparison with 2D sheets, higher ZT values can be achieved. Recently, MoS₂ nanoribbons with widths varying from tens of nanometers to hundreds of nanometers have been synthesized by electrochemical and chemical methods.^{36,37} More recently, nanoribbons with uniform widths of just 0.35 nm have been formed in MoS₂ sheets under electron irradiation.³⁸ One of the most important obstacles in achieving devices based on low-dimensional MoS₂ is to develop a method leading to a large-scale and uniform growth. There have been many efforts toward this goal using various chemical vapor deposition (CVD) methods such as sulfurization of metal or metal compounds^{39,40} or CVD based on solid precursors (such as MoO₃ or MoCl₅).^{41,42} In all these cases, uniformity of the grown films has been a challenge. More recently, a successful uniform monolayer growth of MoS₂ has been reported using the metal organic CVD (MOCVD) method.⁴³ This achievement makes it more important than before to investigate the thermoelectric properties of 1D monolayer MoS₂ nanoribbons. Recently, the thermoelectric properties of MoS₂ nanoribbons have been studied in a DFT framework with relaxation time approximation.⁴⁴ Authors have reported a high value of $ZT \approx 3$ requiring a small amount of Fermi-level shift. Based on a ballistic transport regime, in which no scattering mechanism has been considered, it has been shown in this study that it is indeed possible to obtain a high value of $ZT \approx 3$ –4 but with a much higher Fermi-level shift. We have also considered the effect of nanoribbon defects, such as edge roughness and sulfur vacancies, on its thermoelectric behavior.

COMPUTATIONAL APPROACH

The computational model is based on DFT using a non-equilibrium Green's function (NEGF) method⁴⁵ implemented in the QuantumWise ATK software package. ^aPrior to performing each electronic and phonon calculation, the super-cells have been relaxed to maximum force and stress of 0.05 eV/Å and 0.05 eV/Å³, respectively. The generalized gradient approximation (GGA) exchange correlation, double-zeta polarized (DZP) basis set, mesh cut-off energy of 75 Ha and 10 × 10 × 10 k-point grid is used for relaxation calculations. A large vacuum spacing of at least 20 Å is added in each side of the nanoribbons to hinder the effect of periodic images. The Landauer-Buttiker⁴⁶ formula is used to calculate transport coefficients of the system from Green's function. This formalism is correct in the absence of inelastic scattering and phase-changing mechanisms. In the DFT calculations, Monkhorst–

Pack k-grid⁴⁷ of $1 \times 1 \times 100$ and DZP basis set with density mesh cut-off of 10 Ha is used for super cells within localized density approximation (LDA).

For the electronic transport calculation, the structure is comprised of a channel region and two electrodes. These electrodes are semi-infinite, defect-free MoS₂ nanoribbons with periodic boundary condition. The retarded Green's function of channel is calculated as⁴⁸

$$G(E) = [(E + i0^+)I - H - \Sigma_L - \Sigma_R]^{-1} \quad (1)$$

where H is the channel Hamiltonian matrix and $\Sigma_{L(R)}$ is the self-energy due to the semi-infinite left(right) electrode. Electronic transmission per spin through the channel region is obtained as

$$T_e(E) = \text{tr}[\Gamma_L(E) \cdot G(E) \cdot \Gamma_R(E) \cdot G^+(E)] \quad (2)$$

in which $\Gamma_{L(R)}(E) = -2 \text{Im}(\Sigma_{L(R)})$ is the broadening function of the left(right) electrode and G^+ is the advanced Green's function.

Carrier transport properties are calculated by a ballistic transport approach under a linear response regime. The electrical current I in this regime is given by⁴⁶

$$I = \frac{2q}{h} \int dE \cdot T_e(E) \cdot \{f_L(E, \mu_L) - f_R(E, \mu_R)\} \quad (3)$$

in which the factor of two counts for spin degeneracy, q is the electrical charge, h is the Planck's constant, $T_e(E)$ is the electronic transmission spectrum, $\mu_{L(R)}$ is the chemical potential of the left(right) electrode, and $f_{L(R)}(E, \mu_{L(R)})$ is the Fermi distribution of the left(right) electrode. The Fermi distribution function depends on both the chemical potential and the temperature. In the linear response regime, it is assumed that the system is biased with an infinitesimal voltage drop and temperature gradient. As a result, Eq. 3 will be reduced to

$$I = \frac{2q}{h} \Delta\mu \int dE \cdot T(E) \cdot \frac{\partial f}{\partial \mu} + \frac{2q}{h} \Delta T \int dE \cdot T(E) \cdot \frac{\partial f}{\partial T} \quad (4)$$

where $\Delta\mu$ and ΔT are infinitesimally small. We are interested in the electrical response of monolayer MoS₂ ACNRs to the pure temperature gradient, i.e. there is no voltage bias applied to the electrodes in our simulations, and therefore, $\Delta\mu = 0$ and Eq. 4 will reduce to

$$I = \frac{2q}{h} \Delta T \int dE \cdot T(E) \cdot \frac{\partial f}{\partial T} \quad (5)$$

The electrical conductance (G), Seebeck coefficient (S), and electronic contribution to thermal conductance (κ_e) are calculated by using electronic transmission spectrum as follows

$$G = q^2 L_0 \quad (6)$$

$$S = \frac{L_1}{qTL_0} \quad (7)$$

$$\kappa_e = \frac{1}{T} \left(L_2 - \frac{L_1^2}{L_0} \right) \quad (8)$$

where L_n is expressed as

$$L_n = \frac{2}{h} \int dE \cdot T(E) \cdot \left\{ -\frac{\partial f(E, \mu)}{\partial E} \right\} \cdot (E - \mu)^n \quad (9)$$

Phonon calculations are performed based on parameterization of the Stillinger–Weber potential⁴⁹ for MoS₂²⁸ as implemented in the QuantumWise ATK package. Phonon thermal conductance (κ_{ph}) can be calculated as

$$\kappa_{\text{ph}} = \lim_{\Delta T \rightarrow 0} \frac{\frac{1}{h} \int_0^\infty dE \cdot T_{\text{ph}}(E) \cdot E \cdot \{B(E, T_L) - B(E, T_R)\}}{\Delta T} \quad (10)$$

where $T_{\text{ph}}(E)$ is the phonon transmission spectrum, $B(E, T_{L(R)})$ is the Bose–Einstein distribution of the left(right) electrode, $T_{L(R)}$ is the temperature of the left(right) electrode, and E is the energy of transmitted phonons. In the linear response regime, temperature bias on the electrodes is infinitesimally small. As a result, Eq. (10) becomes

$$\kappa_{\text{ph}} = \frac{1}{h} \int_0^\infty dE \cdot T_{\text{ph}}(E) \cdot E \cdot \left(-\frac{\partial B(E, T)}{\partial T} \right) \quad (11)$$

The thermoelectric figure of merit can be readily obtained using these parameters as

$$ZT = \frac{GS^2T}{\kappa_e + \kappa_{\text{ph}}} \quad (12)$$

It is worth mentioning that the phonon calculations in this paper are performed in the absence of any phonon decaying mechanisms. As a result, these calculations set the upper limit for the phonon thermal conductance. In real situations, however, there would be a few mechanisms such as scattering centers, crystal imperfectness, surface roughness, etc., which tend to suppress phonon conduction; therefore, ZT values calculated in this study are minimum values of what actually can be achieved by monolayer MoS₂ ACNRs.

RESULTS AND DISCUSSION

The atomic structure of the monolayer MoS₂ ACNRs, as shown in Fig. 1, can be considered as monolayer MoS₂ tailored along the armchair direction. Nanoribbons with various widths can be identified by a number of zigzag chains across the ACNR, as illustrated in Fig. 1, and are labeled as N-ACNR. In this study, we focus on eight different

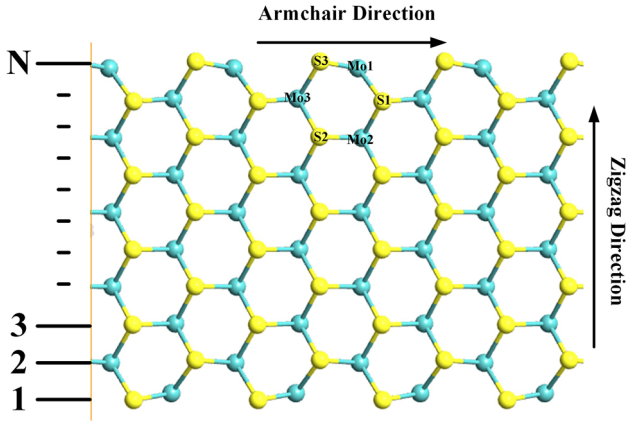


Fig. 1. Atomic structure of monolayer MoS₂ N-ACNR. Armchair and zigzag direction are shown in the figure. N , the width identifier, is the number of atoms in the zigzag direction across the nanoribbon. Atoms at the edge of the nanoribbon are distorted from their original configuration after relaxing the structure.

widths of ACNRs, $N = 3-10$. Widths of nanoribbons investigated in this work change from 5.71 Å for 3-ACNR to 16.31 Å for 10-ACNR. Upon relaxation and geometry optimization, the atomic structure reconstructs itself. This reconstruction is more pronounced at the edges of the nanoribbon than at its center. To have a fair idea about the extent of this reconstruction, Fig. 1 shows the relaxed structure of 10-ACNR with labeled atoms at the edge of the nanoribbon. It is found that the $Mo1-S3$ bond length decreases from 2.42 Å to 2.34 Å, the $Mo1-S1$ bond length increases from 2.42 Å to 2.46 Å, and the $Mo1-Mo3$ bond length decreases from 3.16 Å to 2.97 Å. In addition, the bond angle of $Mo1-S3-Mo3$ decreases from 81.63 to 75.78 degrees. Similar reconstruction, not shown here, happens for all ACNRs investigated in this study. This reconstruction is important in determining the electronic and transport properties of nanoribbons since the energy states around the Fermi level are mainly composed by edge states.⁵⁰

All of the monolayer MoS₂ ACNRs that are studied in this work are semiconducting, which is in agreement with previous reports.^{51,52} Figure 2 depicts the band gap values of these semiconducting MoS₂ ACNRs versus N , the width identifier. It should be noted that the band gap values of ACNRs are much smaller than those of bulk MoS₂ (1.2 eV)¹⁰ and monolayer MoS₂ (1.8 eV).¹¹ This behavior cannot be explained by the well-known quantum confinement effects, since those effects tend to increase the band gap. Atoms at the edge of nanoribbons, introduce energy states in the middle of the band gap near both valence and conduction bands, and therefore narrow the band gap.⁷ In addition, Fig. 2 illustrates that the band gap values exhibit some sort of oscillation as a function of the nanoribbon's width. It can be seen that nanoribbons with $N = 3p - 1$, p being an integer, have a larger band gap than the neighboring ones. The same behavior

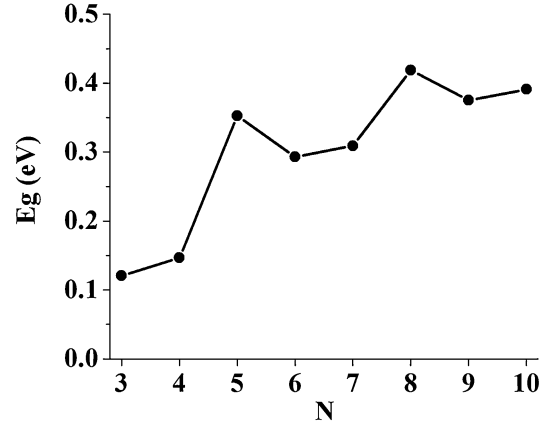


Fig. 2. Band gap of monolayer MoS₂ ACNR versus N at $\mu = 0$. Band gap increases as ACNRs widen except for those with $N = 3$, $p - 1$ which have larger band gaps than the neighboring ones.

has been reported for the graphene armchair nanoribbons⁵³ and silicon armchair nanoribbons,⁵⁴ and can be generalized as a robust signature of the nanoribbons with armchair edges.

First, we investigated the thermoelectric properties of perfect and defect-free monolayer MoS₂ ACNRs. Electronic components of a thermoelectric figure of merit can be readily obtained by appropriate integration of transmission function, as discussed in previous section. These integrations involve the Fermi distribution function; therefore, the electronic transport coefficients depend on the chemical potential and temperature. The chemical potential can shift into positive or negative values by either inducing a gate voltage across the nanoribbon or doping it. In the rigid band picture, positive and negative values of chemical potentials correspond to n -type and p -type doping, respectively. The Seebeck coefficient as a function of the chemical potential (μ) and for different temperatures for all ACNRs is depicted in Fig. 3. As can be seen from Eq. (7), the Seebeck coefficient is inversely proportional to temperature, and as temperature increases, the peak value of the Seebeck coefficient decreases. The Seebeck coefficient for ACNRs, shown in Fig. 3, follows the same trend. Further study of Fig. 3 reveals that the Seebeck coefficient of each ACNR has three peaks; one around $\mu = 0$, one for positive μ and one for negative μ values. Peaks of the Seebeck coefficient correspond to the maximum value of the transmission-coefficient-weighted average of $(E - \mu)$, see Eq. (7), which occurs at energies around the middle of the band gaps of transmission coefficient,⁵⁵ and the absolute values of these peaks increase as the band gap increases.⁵⁶ Band gap values at $\mu = 0$ are illustrated in Fig. 2, and it can be seen that peaks of the Seebeck coefficient at $\mu = 0$ follow the same trend as the band gap values. As the nanoribbons get wider, the band gap increases, except for 5-ACNR and 8-ACNR, which have a larger band gap

Monolayer MoS₂ Nanoribbons as a Promising Material for Both *n*-type and *p*-type Legs in Thermoelectric Generators

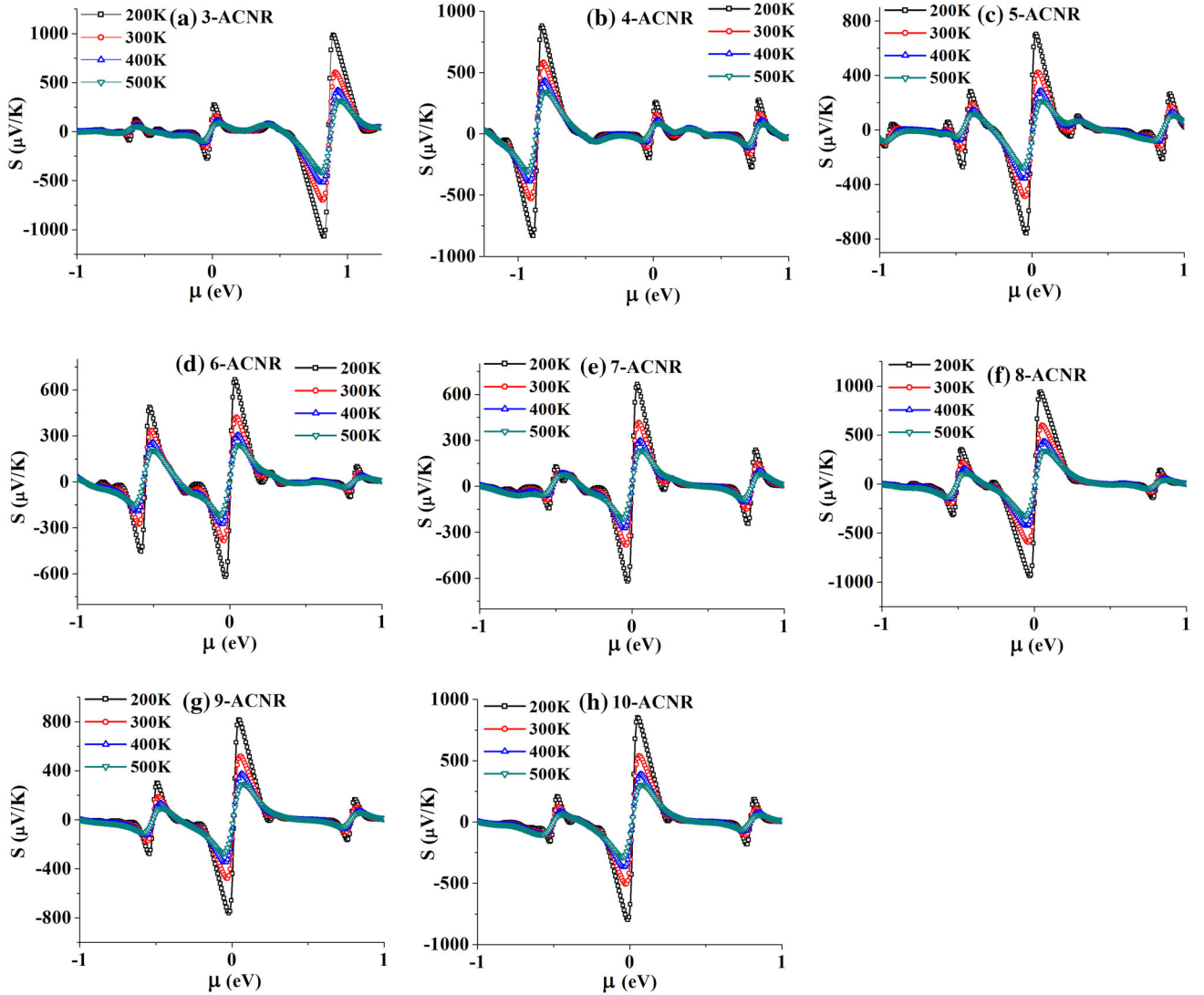


Fig. 3. Seebeck coefficient of N-ACNRs for $N = 3$ –10 versus the chemical potential for different temperatures in (a) through (h).

than the neighboring nanoribbons, and hence the Seebeck peaks around $\mu = 0$ also increase. Transmission spectra of three ACNRs that exhibit distinctive Seebeck coefficient profiles are depicted in Fig. 4 in order to further clarify how the band gap values affect the Seebeck coefficient profile. The transmission spectrum of each ACNR has three band gaps. There is a band gap at $\mu = 0$ (center-gap), a band gap at positive μ values (positive- μ gap), and a band gap at negative μ values (negative- μ gap). One of these gaps is wider than the other two in the transmission spectrum of each ACNR. As is depicted in Fig. 4, the positive- μ gap, negative- μ gap, and center gap are the widest gaps for 3-ACNR, 4-ACNR, and 10-ACNR, respectively. The Seebeck coefficient profiles, illustrated in Fig. 3, follow the same trend, as their peak values are higher where

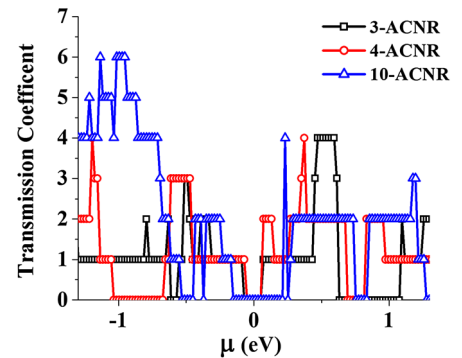


Fig. 4. Transmission spectra for N-ACNRs with $N = 3, 4$, and 10. Each transmission spectrum comprised of three band gaps. For 10-ACNR, the band gap at $\mu = 0$ is larger than the other two. For 3-ACNR and 4-ACNR, however, the band gap for *n*-type and *p*-type (in rigid band picture) is the largest, respectively.

the gap is wider in their corresponding transmission spectra.

Electrical conductance (G) and electronic thermal conductance (κ_e) are the other two electronic transport coefficients that can be obtained from the transmission spectra. These two transport coefficients for 3-ACNR, 4-ACNR, and 10-ACNR are illustrated in Fig. 5. Panels (a) and (b) show G and κ_e at room temperature, respectively. The profiles for both of these transport coefficients follow the same trend as their corresponding transmission spectra versus chemical potential. As the chemical potential moves into conduction or valence bands, there are more carriers to be conducted thermally and electrically; therefore, both G and κ_e increase. Also, when the chemical potential enters the band gaps, both G and κ_e are supposed to be zero. However, this is not the case when the chemical potential enters small band gaps in transmission spectra. As is depicted for 3-ACNR and 4-ACNR in Fig. 5, the center gaps are in the order of $5 K_B T$ and the Fermi distribution function excites some of the transmission channels even when the chemical potential is well inside these band gaps. As a result, when the chemical potential moves into these small band gaps, electrical and thermal conductance decreases but does not drop to zero. Similar behavior can be seen at the positive- μ gap and negative- μ gap for 10-ACNR. Panels (c) and (d) of Fig. 5

illustrate G and κ_e of 10-ACNR versus the chemical potential for different temperatures. It can be seen from panel (c) that for the center gap, electrical conductance does not change very much as the temperature increases, while at the positive- μ gap and negative- μ gap, it changes more significantly. This behavior is due to broadening of the Fermi distribution function. For higher temperatures, Fermi distribution is broader and excites more states in neighboring bands than at lower temperatures. This effect is more pronounced for smaller gaps as compared to larger gaps. The electronic thermal conductance of 10-ACNR for different temperatures is illustrated in panel (d) of Fig. 5. At higher temperatures more carriers will be conducted thermally, and electronic thermal conductance increases.

Phonon thermal conductance (κ_{ph}) has been obtained by parametrization of the Stillinger–Weber potential for MoS_2 . In contrast to κ_e , κ_{ph} is not affected by shifting the chemical potential and is constant as μ changes. Phonon thermal conductance increases as temperature increases, as is shown in panel (a) of Fig. 6 (not shown for all ACNRs). In addition, it can be noted that the rate at which κ_{ph} increases versus temperature is higher for wider nanoribbons as compared to narrower nanoribbons. Moreover, κ_{ph} at room temperature for all ACNRs is illustrated in panel (b) of Fig. 6. As nanoribbons get

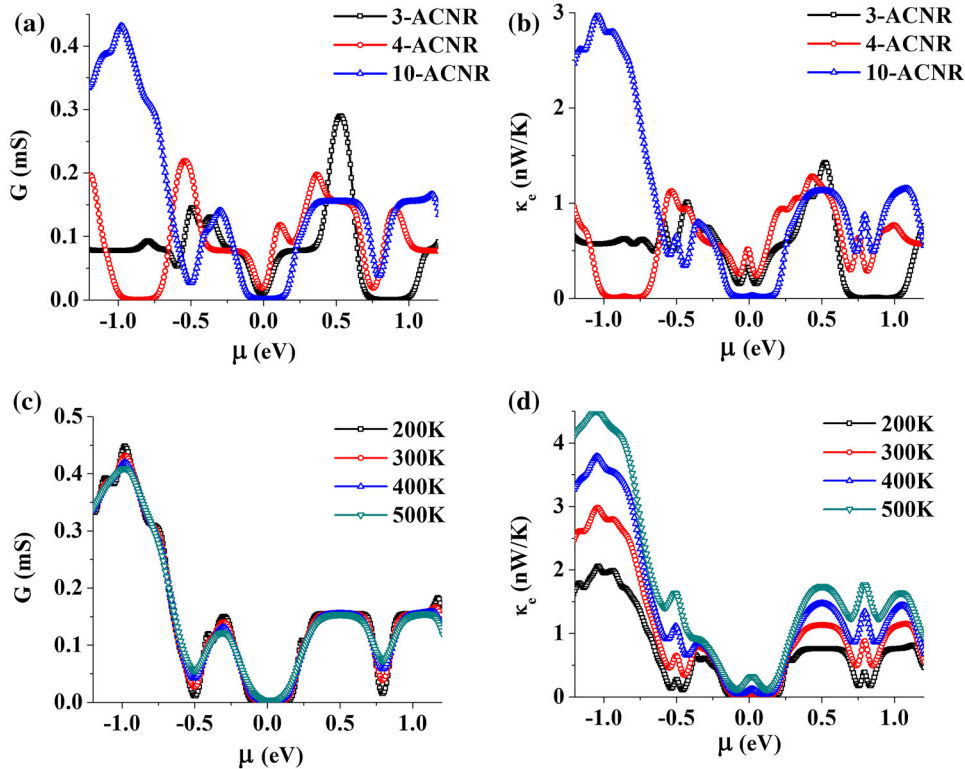


Fig. 5. Electrical conductance and electronic thermal conductance for N-ACNRs with $N = 3, 4,$ and 10 versus chemical potential in panels (a) and (b), respectively. Electrical conductance and electronic thermal conductance of 10-ACNR versus chemical potential for different temperatures are illustrated in (c) and (d), respectively.

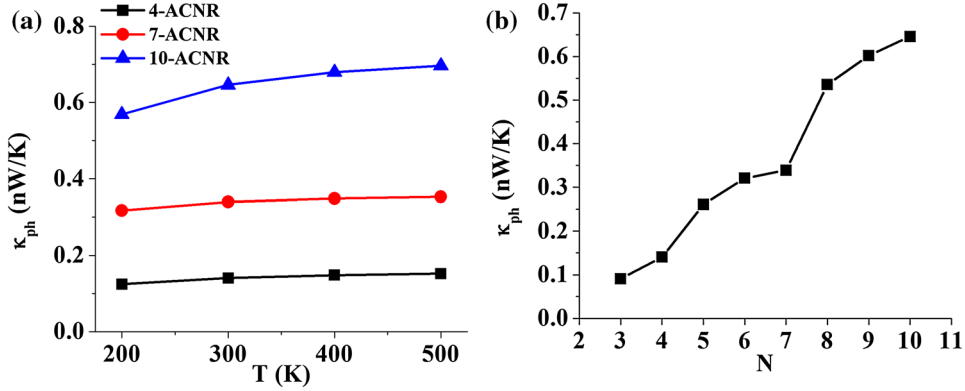


Fig. 6. (a) Phonon thermal conductance for N-ACNR with $N = 4, 7,$ and 10 versus temperature. Rate of increase in phonon thermal conductance versus temperature is more for wider ACNRs compared to narrower ones. (b) Phonon thermal conductance at room temperature for all ACNRs.

wider, κ_{ph} increases. In narrower nanoribbons, there are fewer channels to conduct heat by phonons and the effect of edge phonon scattering is more profound as compared to wider nanoribbons. As nanoribbons widen, there are more available channels for phonons to conduct heat and the effect of boundary scattering decreases.⁵⁷

Now that all the parameters have been computed, the thermoelectric figure of merit, $ZT = \frac{GS^2}{\kappa_e + \kappa_{ph}} T$, can readily be obtained. ZT values of all monolayer MoS₂ ACNRs as a function of the chemical potential position and for various temperatures have been illustrated in Fig. 7. The Seebeck coefficient, as can be seen from Fig. 3, reaches its maximum value at energies around $\pm K_B T$ of the middle of each band gap, and as the chemical potential approaches the conduction or valence subbands, it rapidly drops. In contrast to the Seebeck coefficient, electrical conductance increases when the chemical potential moves from the band gaps and approaches the conduction or valence subbands. Therefore, ZT peaks are located at some optimized energy at which these two competing factors, in terms of GS^2 , reaches its maximum value. It is expected that ZT increases approximately linearly as temperature increases.³⁴ However, further study of Fig. 7 reveals that it is not always the case in our results. Each ZT profile, similar to the Seebeck coefficient profiles, has three major peaks: one around the middle of the center gap and two around the middle of the positive- μ and negative- μ gaps. It can be seen that the ZT peaks that are located within the small band gaps, i.e. the positive- μ gap of 3-ACNR or negative- μ gap of 4-ACNR, decrease as temperature increases. This behavior can be explained by the temperature dependence of the electrical conductance at these small band gaps. The Seebeck coefficient is inversely proportional to temperature. As a result, the discrepancy of the temperature dependence of ZT peaks at smaller band gaps should have been caused by the electrical conductance. It has been explained earlier that as the chemical potential moves into small band gaps, electrical conductance

is reduced but this drop in electrical conductance is lessened as temperature increases (see Fig. 5). This behavior was explained by the broadening of the Fermi distribution function. It can be noted from Fig. 7 that for ZT peaks located at energies corresponding to larger band gaps, the maximum value increases as the temperature increases. In order to clarify this behavior, the maximum value of ZT located around $\mu = 0$ for both *p*-type and *n*-type (in the rigid band picture) MoS₂ ACNRs is depicted in Fig. 8 for two temperatures. It has already been discussed that the band gap at $\mu = 0$ increases as the nanoribbons widen, except for with 5-ACNR and 8-ACNR, for which the band gap is larger than their neighboring ones. It has been shown that for 3-ACNR and 4-ACNR, both ZT values of *p*-type and *n*-type at $T = 200$ K are higher than those at $T = 500$ K, and as N increases and therefore the band gap increases, ZT values at $T = 500$ K become higher than those at $T = 200$ K. This study has shown that ZT values larger than unity can be achieved by MoS₂ ACNRs. For *n*-type nanoribbons, a ZT value of 2.82 at room temperature and $\mu = 0.67$ eV can be achieved using 3-ACNR. For *p*-type nanoribbons, a ZT value of 2.16 at room temperature and $\mu = -0.7$ eV can be achieved using 4-ACNR. At higher temperatures ZT values on the order of 3 and 4 can be obtained. These ZT values are far superior to those of bulk or monolayer and multi-layer sheets of MoS₂.^{29,32,34} The amount of Fermi level shift to obtain the maximum possible ZT of 3-ACNR and 4-ACNR translates to a degenerate doping level of monolayer MoS₂ ACNRs. Degenerate doping of TMDCs using alkali metals⁵⁸ and chemical molecules^{59,60} to achieve both *p*-type and *n*-type behavior has been already reported.

In addition to perfect MoS₂ ACNRs, the effect of two types of defects on the thermoelectric properties of MoS₂ nanoribbons was also studied: sulfur vacancy and edge roughness. The reasoning behind incorporating these defects is to increase phonon scattering by inducing lattice defects without tremendously degrading electrical conductance.

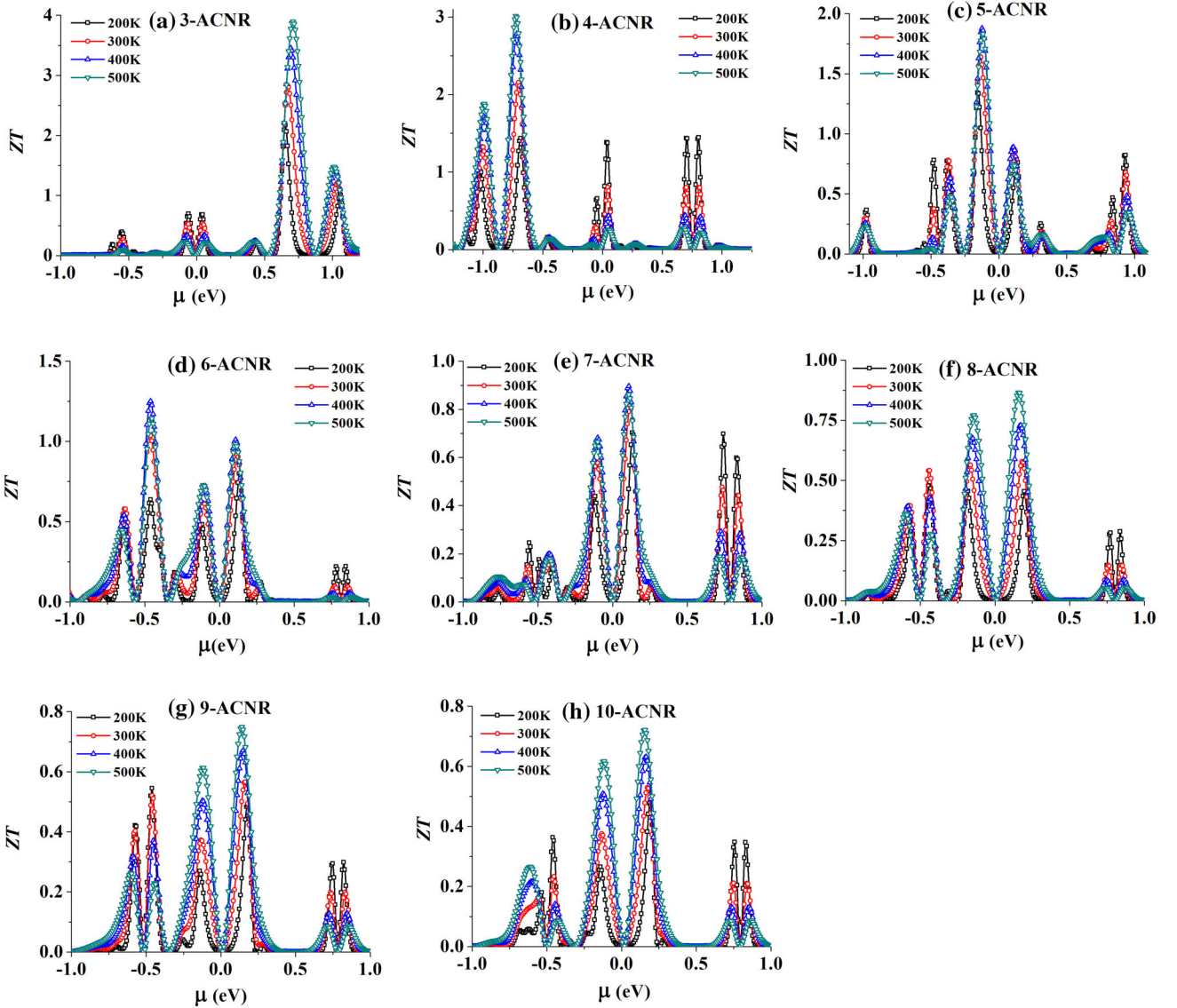


Fig. 7. ZT value of N-ACNRs for $N = 3$ –10 versus the chemical potential for different temperatures in (a) through (h).

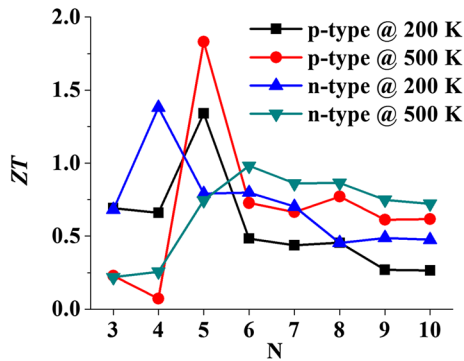


Fig. 8. Maximum value of p -type and n -type ZT peaks for all ACNRs for $T = 200$ K and $T = 500$ K at $\mu = 0$.

For both of these defects 10-ACNR has been adopted as the framework. The widest nanoribbon is chosen because the effect of defects on its electrical

conductance is less than that of the narrower nanoribbons. Sulfur vacancy is formed by removing a sulfur atom from the center of the nanoribbon, and edge roughness has been formed by deliberately degrading the perfect structure of the nanoribbon at its edge (illustrated in inset of panel (a) of Fig. 9). Both of these defect-induced structures have been relaxed using the same relaxation parameters that have been discussed in a previous section. The effect of these defects on the transport coefficients at room temperature is shown in Fig. 9. Panel (a) shows the transmission spectra of defect-free 10-ACNR as well as of those with sulfur vacancy and edge roughness. Due to translational symmetry breaking in defect-induced ACNRs, transmission spectra have been deviated from a stepwise profile to smoother ones. Moreover, it can be seen that both of the defects have decreased the transmission coefficients of

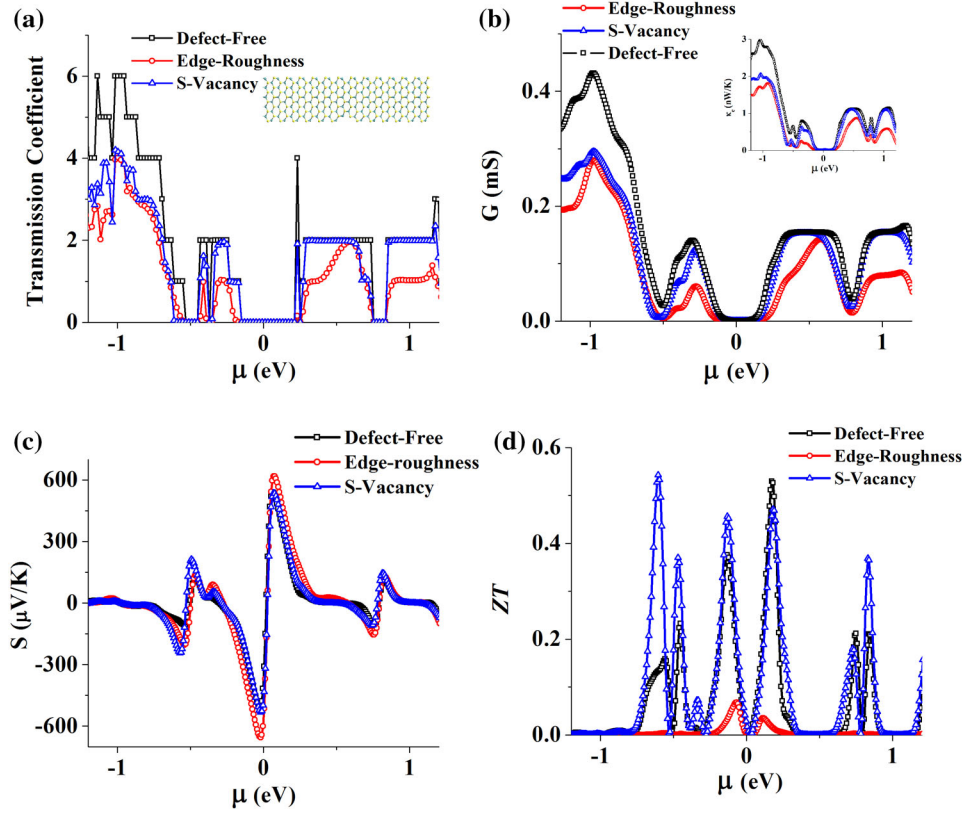


Fig. 9. Effects of sulfur vacancy and edge roughness on the thermoelectric properties of 10-ACNR have been studied and compared with those of the perfect nanoribbon; (a) transmission spectra, inset shows atomic structure of 10-ACNR with edge roughness, (b) electrical conductance; inset depicts electronic thermal conductance, (c) Seebeck coefficient, and (d) ZT.

nanoribbons, which leads to a drop in electrical conductance and electronic thermal conductance of nanoribbons, as is depicted in panel (b) and its inset. Also, it is evident that carrier conductance, both thermally and electrically, has been degraded more by edge roughness as compared to sulfur vacancy. Further study of transmission spectra reveals that edge roughness affects edge conduction as expected, which corresponds to higher valence and lower conduction subbands much more significantly than does sulfur vacancy. In contrast to carrier conductance, changes in the Seebeck coefficient of ACNR with sulfur vacancy are negligible as compared to those of perfect ACNR. Nanoribbons with edge roughness show an increase in Seebeck coefficient peaks around $\mu = 0$; however, for lower valence subbands, the Seebeck coefficient has been decreased in comparison with perfect ACNR. This can be explained by the fact that the Seebeck coefficient is proportional to the transmission-weighted average of $(E - \mu)$. At a given temperature, in order to have a higher Seebeck coefficient, the transport of carriers with lower $(E - \mu)$ should be suppressed. By inducing edge roughness, the sharp and stepwise increase of transmission coefficients at the edge's valence and conduction subbands have been smoothed, and the transport of those carriers has been suppressed compared to

carriers with higher energies. This situation has not happened in the case of ACNRs with sulfur vacancy, and the edges of valence and conduction subbands have the same stepwise shape as those in perfect ACNR. In addition to electrical transport coefficients, defects have affected phonon thermal conductance as well. In the case of perfect ACNR $\kappa_{ph} = 0.65$ nW/K, sulfur vacancy reduced it to 0.5 nW/K and edge roughness reduced it further to 0.36 nW/K. It can be noted from panel (d) of Fig. 9 that the drop in phonon thermal conductance and the increase in Seebeck coefficient in ACNRs with rough edges have been marginalized by a drop in the electrical conductance, and the ZT has been reduced tremendously as compared to perfect ACNR. However, sulfur vacancy, which has not degraded the electrical conductance as much as the edge roughness, was shown to improve the ZT in some subbands. ZT values for *p*-type ACNR have been boosted by sulfur vacancy compared to those of perfect ACNR.

CONCLUSION

Thermoelectric properties of monolayer MoS₂ ACNRs in the ballistic transport regime in linear approximation are investigated in this work. Nanoribbons are identified by the number of zigzag

chains across them and denoted as N-ACNR. The effect of the size of nanoribbons on their thermoelectric behavior by considering $N = 3-10$ has been studied. Transmission spectra of ACNRs are comprised of edge subbands for both electrons and holes. This leads to the existence of three gaps in transmission spectra. It has been shown that the band gap at $\mu = 0$ increases as ACNRs widens, except for those with $N = 3, p - 1$, in which p is an integer that has higher band gaps than neighboring ones. As the width of ACNRs increases, the Seebeck coefficient and ZT around $\mu = 0$ both increase. Phonon thermal conductance decreases as ACNRs narrow due to an increased impact of phonon edge scattering. As a result, the maximum ZT values that can be achieved by narrow ACNRs are higher than the wider ones. The effect of sulfur vacancy and edge roughness on thermoelectric properties is also investigated. It is found that, although edge roughness will reduce phonon thermal conductance, the degradation in electrical conductance leads to a tremendous drop in ZT. In contrast to edge roughness, a sulfur vacancy reduces the phonon thermal conductance without degrading electrical conductance as much as edge roughness, leading to an increased ZT value at some energies. It has been shown that ZT values as high as $ZT = 4$ in 3-ACNR for n -type material and $ZT = 3$ in 4-ACNR for p -type material at $T = 500$ K can be achieved. The possibility of gaining high ZT values for both n -type and p -type material makes monolayer MoS₂ ACNRs a promising candidate in future thermoelectric generators.

REFERENCES

1. K.S. Novoselov, A.K. Geim, S.V. Morozov, D. Jiang, Y. Zhang, S.V. Dubonos, I.V. Grigorieva, and A.A. Firsov, *Science* 306, 5696 (2004).
2. Y. Zhang, Y.-W. Tan, H.L. Stormer, and P. Kim, *Nature* 438, 7065 (2005).
3. A.C. Ferrari, J.C. Meyer, V. Scardaci, C. Casiraghi, M. Lazzeri, F. Mauri, S. Piscanec, D. Jiang, K.S. Novoselov, S. Roth, and A.K. Geim, *Phys. Rev. Lett.* 97, 18 (2006).
4. K.S. Novoselov, A.K. Geim, S.V. Morozov, D. Jiang, M.I. Katsnelson, I.V. Grigorieva, S.V. Dubonos, and A.A. Firsov, *Nature* 438, 7065 (2005).
5. R.F. Frindt, *J. Appl. Phys.* 37, 4 (1966).
6. A. Schumacher, L. Scandella, N. Kruse, and R. Prins, *Surf. Sci.* 289, 1 (1993).
7. Y. Li, Z. Zhou, S. Zhang, and Z. Chen, *J. Am. Chem. Soc.* 130, 49 (2008).
8. L. Kou, C. Tang, Y. Zhang, T. Heine, C. Chen, and T. Frauenheim, *J. Phys. Chem. Lett.* 3, 20 (2012).
9. C. Ataca, H. Sahin, E. Akturk, and S. Ciraci, *J. Phys. Chem. C* 115, 10 (2011).
10. K.K. Kam and B.A. Parkinson, *J. Phys. Chem.* 86, 4 (1982).
11. K.F. Mak, C. Lee, J. Hone, J. Shan, and T.F. Heinz, *Phys. Rev. Lett.* 105, 13 (2010).
12. B. Radisavljevic, A. Radenovic, J. Brivio, V. Giacometti, and A. Kis, *Nat. Nanotechnol.* 6, 3 (2011).
13. E. Gourmelon, J.C. Bernede, J. Pouzet, and S. Marsillac, *J. Appl. Phys.* 87, 3 (2000).
14. B. Radisavljevic, M.B. Whitwick, and A. Kis, *ACS Nano* 5, 12 (2011).
15. S. Yu, K. Eshun, H. Zhu, and Q. Li, *Sci. Rep.* (2015). doi: 10.1038/srep12854.
16. A. Kuc, N. Zibouche, and T. Heine, *Phys. Rev. B* 83, 24 (2011).
17. Y. Pei, A. LaLonde, S. Iwanaga, and G.J. Snyder, *Energy Environ. Sci.* 4, 6 (2011).
18. K. Biswas, J. He, I.D. Blum, C.-I. Wu, T.P. Hogan, D.N. Seidman, V.P. Dravid, and M.G. Kanatzidis, *Nature* 489, 7416 (2012).
19. L.D. Hicks and M.S. Dresselhaus, *Phys. Rev. B* 47, 19 (1993).
20. L.D. Hicks and M.S. Dresselhaus, *Phys. Rev. B* 47, 24 (1993).
21. M.S. Dresselhaus, G. Chen, M.Y. Tang, R.G. Yang, H. Lee, D.Z. Wang, Z.F. Ren, J.-P. Fleurial, and P. Gogna, *Adv. Mater.* 19, 8 (2007).
22. D.M. Rowe, V.S. Shukla, and N. Savvides, *Nature* 290, 765 (1981).
23. A.I. Hochbaum, R. Chen, R.D. Delgado, W. Liang, E.C. Garnett, M. Najarian, A. Majumdar, and P. Yang, *Nature* 451, 7175 (2008).
24. X. Shi, L. Chen, J. Yang, and G.P. Meisner, *Appl. Phys. Lett.* 84, 2301 (2004).
25. R. Mansfield and S.A. Salam, *Proc. Phys. Soc. Sect. B* 66, 5 (1953).
26. M. Buscema, M. Barkelid, V. Zwiller, H.S. van der Zant, G.A. Steele, and A. Castellanos-Gomez, *Nano Lett.* 13, 2 (2013).
27. X. Liu, G. Zhang, Q.-X. Pei, and Y.-W. Zhang, *Appl. Phys. Lett.* 103, 13 (2013).
28. J.-W. Jiang, H.S. Park, and T. Rabczuk, *J. Appl. Phys.* 114, 6 (2013).
29. G. Huai-Hong, Y. Teng, T. Peng, and Z. Zhi-Dong, *Chin. Phys. B* 23, 1 (2014).
30. M.K. Agarwal and L.T. Talele, *Solid State Commun.* 59, 8 (1986).
31. S.G. Thakurta and A.K. Dutta, *J. Phys. Chem. Solids* 44, 5 (1983).
32. H. Guo, T. Yang, P. Tao, Y. Wang, and Z. Zhang, *J. Appl. Phys.* 113, 1 (2013).
33. J.-W. Jiang, X. Zhuang, and T. Rabczuk, *Sci. Rep.* 3, 2209 (2013).
34. A. Arab and Q. Li, *Sci. Rep.* 5, 1306 (2015).
35. D. Wickramaratne, F. Zahid, and R.K. Lake, *J. Chem. Phys.* 140, 12 (2014).
36. Q. Li, E.C. Walter, W.E. Van der Veer, B.J. Murray, J.T. Newberg, E.W. Bohannon, J.A. Switzer, J.C. Hemminger, and R.M. Penner, *J. Phys. Chem. B* 109, 8 (2005).
37. Q. Li, J.T. Newberg, E.C. Walter, J.C. Hemminger, and R.M. Penner, *Nano Lett.* 4, 2 (2004).
38. X. Liu, T. Xu, X. Wu, Z. Zhang, J. Yu, H. Qiu, J.-H. Hong, C.-H. Jin, J.-X. Li, X.-R. Wang, L.-T. Sun, and W. Guo, *Nat. Commun.* 4, 3121 (2013).
39. Y.-C. Lin, W. Zhang, J.-K. Huang, K.-K. Liu, Y.-H. Lee, C.-T. Liang, C.-W. Chu, and L.-J. Li, *Nanoscale* 4, 20 (2012).
40. I. Song, C. Park, M. Hong, J. Baik, H.-J. Shin, and H.C. Choi, *Angew. Chem. Int. Ed.* 53, 5 (2014).
41. S. Najmaei, Z. Liu, W. Zhou, X. Zou, G. Shi, S. Lei, B.I. Yakobson, J.-C. Idrobo, P.M. Ajayan, and J. Lou, *Nat. Mater.* 12, 8 (2013).
42. A.M. van der Zande, P.Y. Huang, D.A. Chenet, T.C. Berkelbach, Y. You, G.-H. Lee, T.F. Heinz, D.R. Reichman, D.A. Muller, and J.C. Hone, *Nat. Mater.* 12, 6 (2013).
43. K. Kang, S. Xie, L. Huang, Y. Han, P.Y. Huang, K.F. Mak, C.-J. Kim, D. Muller, and J. Park, *Nature* 520, 7549 (2015).
44. D.D. Fan, H.J. Liu, L. Cheng, P.H. Jiang, J. Shi, and X.F. Tang, *Appl. Phys. Lett.* 105, 13 (2014).
45. M. Brandbyge, J.-L. Mozos, P. Ordejón, J. Taylor, and K. Stokbro, *Phys. Rev. B* 65, 16 (2002).
46. M. Büttiker, Y. Imry, R. Landauer, and S. Pinhas, *Phys. Rev. B* 31, 10 (1985).
47. H.J. Monkhorst and J.D. Pack, *Phys. Rev. B* 13, 12 (1976).
48. S. Datta, *Quantum Transport: Atom to Transistor* (Cambridge: Cambridge University Press, 2005), pp. 285–312.
49. F.H. Stillinger and T.A. Weber, *Phys. Rev. B* 31, 8 (1985).

Monolayer MoS₂ Nanoribbons as a Promising Material for Both *n*-type and *p*-type Legs in Thermoelectric Generators

50. Y. Cai, G. Zhang, and Y.-W. Zhang, *J. Am. Chem. Soc.* 136, 17 (2014).
51. H. Pan and Y.-W. Zhang, *J. Mater. Chem.* 22, 15 (2012).
52. A.R. Botello-Méndez, F. Lopez-Urias, M. Terrones, and H. Terrones, *Nanotechnology* 20, 32 (2009).
53. H. Zheng, Z.F. Wang, T. Luo, Q.W. Shi, and J. Chen, *Phys. Rev. B* 75, 16 (2007).
54. L. Pan, H.J. Liu, X.J. Tan, H.Y. Lv, J. Shi, X.F. Tang, and G. Zheng, *Phys. Chem. Chem. Phys.* 14, 39 (2012).
55. Y. Ouyang and J. Guo, *Appl. Phys. Lett.* 94, 26 (2009).
56. J.-W. Jiang, J.-S. Wang, and B. Li, *J. Appl. Phys.* 109, 1 (2011).
57. Z. Guo, D. Zhang, and X.-G. Gong, *Appl. Phys. Lett.* 95, 16 (2009).
58. H. Fang, M. Tosun, G. Seol, T.C. Chang, K. Takei, J. Guo, and A. Javey, *Nano Lett.* 13, 5 (2013).
59. D. Kiriya, M. Tosun, P. Zhao, J.S. Kang, and A. Javey, *J. Am. Chem. Soc.* 136, 22 (2014).
60. H. Fang, S. Chuang, T.C. Chang, K. Takei, T. Takahashi, and A. Javey, *Nano Lett.* 12, 7 (2012).